ChemPubSoc Europe

DOI: 10.1002/cssc.201801968

CHEMSUSCHEM Full Papers

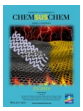

A Large-Sized Reduced Graphene Oxide with Low Charge-Transfer Resistance as a High-Performance Electrode for a Nonflammable High-Temperature Stable Ionic-Liquid-Based Supercapacitor

Li Ma, Qiuming Gao,* Weiqian Tian, Qiang Zhang, Hong Xiao, Zeyu Li, Hang Zhang, and Xuehui Tian[a]

Large-sized reduced graphene oxide prepared was prepared by combined microwave intermittent heating and an extraction process (e.g., 900 W for 10 min (MRG-900-10)) with a lateral size of several micrometers and a thickness of 4–6 monosheets . The MRG-900-10 has a high C/O molar ratio (5.89) and a sp^2 C content of 69.0%, which leads to a fast electronic transmission in the sample. In addition, MRG-900-10 possesses a large specific surface area of 568.2 $m^2 g^{-1}$, which increases the contact surface area between the active material and the electrolyte, thus enhancing the electron and ion transport in the interfaces when used as the electrode material in supercapacitors. MRG-900-10 possesses a low charge-transfer resistance (≈0.36 Ω). Used as the electrode material for a supercapacitor in 6 M KOH aqueous electrolyte, MRG-900-10 produces a high specific capacity of 327.6 F g^{-1} at the current density of 0.5 A g^{-1}. A specific capacity of 248.3 F g^{-1} was obtained at a high current density of 100 A g^{-1}, which indicated its high-rate ability. The initial capacity of 92% can be maintained after 40 000 cycles at 5 A g^{-1}, which indicated its high cycling stability. As for the MRG-900-10 symmetric supercapacitors, the energy densities of 11.0 and 36.2 Wh kg^{-1} were obtained in 6 M KOH aqueous and 1 M tetraethylammonium tetrafluoroborate ($[TEA]BF_4$)/acetonitrile (ACN) electrolytes, respectively. Importantly, a high energy density of 68.6 Wh kg^{-1} was achieved in the nonflammable ionic liquid 1-ethyl-3-methylimidazolium bis(trifluoromethane)sulfonimide ([EMIM][TFSI])/ACN (80 vol% [EMIM][TFSI]), and the supercapacitor was effective from room temperature to 100 °C.

Introduction

Supercapacitors have attracted great attention due to their unique properties, such as high power density, environmental benignity, and so forth.[1,2] However, the main limit for their application is the low energy density, which is an order of magnitude lower than that of batteries.[3] Typically, the energy density of supercapacitors composed of porous activated carbon electrodes in aqueous electrolyte is about 4–5 Wh kg^{-1},[4] which is about one fifth that of lead acid batteries (20–30 Wh kg^{-1}) and much lower than that of lithium ion batteries (≈180 Wh kg^{-1}).[5,6] The carbon-based supercapacitors employ aprotic solvents as the electrolyte solutions, typically acetonitrile (ACN) or carbonate-based solvents such as propylene carbonate, ethylene carbonate.[7] Even though those organic electrolytes have a higher operating voltage than aqueous electrolytes, careful and expensive thermal controls are required for the necessary security requirements caused by the flammability and the high vapor pressure of the electrolytes.[8] Thus, it is essential to construct the suitable electrode materials and optimize the matched electrolytes to produce the efficient and secure supercapacitors with balanced power and energy densities.

Reduced graphene oxide (rGO) as a 2D carbonaceous material, was studied extensively based on its typical characteristics, that is, high electronic conductivity, large surface area, excellent thermal and mechanical stabilities.[9,10] Usually, the rGO materials could be prepared by chemical exfoliation techniques. For example, Feng et al. reported the preparation of rGO by a one-pot low-temperature solution reduction of GO by using a sodium/ammonia solution as the reducing agent.[10] Other chemical methods were also used to obtain rGO, for example, Mullen's group reported a bottom-up method to fabricate graphene nanoribbons on a gold surface from 10,100-dibromo-9,90-bianthryl precursor monomers.[11]

Recently, microwave techniques were chosen to prepare rGO based on the characteristics of internal and volumetric heating in a very short time period. For instance, Ruoff et al. reported the preparation of rGO by applying microwave power to expanding and reducing the GO sheets.[12] When used as the electrode in the supercapacitor, the relatively low specific capacity of 191 F g^{-1} was obtained in 6 M KOH electrolyte.

[a] L. Ma, Prof. Dr. Q. Gao, Dr. W. Tian, Q. Zhang, H. Xiao, Z. Li, H. Zhang, X. Tian
Key Laboratory of Bio-inspired Smart Interfacial Science and Technology of Ministry of Education
Beijing Key Laboratory of Bio-inspired Energy Materials and Devices
School of Chemistry Beihang University
Beijing 100191 (People's Republic of China)
E-mail: qmgao@buaa.edu.cn

Supporting Information and the ORCID identification number(s) for the author(s) of this article can be found under: https://doi.org/10.1002/cssc.201801968.

Thus, high-quality rGO as well as the relevant effective preparative techniques are still urgently needed for improving the electrochemical properties of rGO electrodes.[13] Herein, large-sized rGO nanosheets (denoted as MRG, i.e., microwave-caused rGO) were prepared by microwave heating reduction of GO with *N*,*N*-dimethylacetamide (DMA) as the solvent and ethyl acetate as the precipitant. The optimized MRG has high C/O molar ratio and content of sp^2 C, large specific surface area, and low charge-transfer resistance. Used as the electrode materials of supercapacitors, amazing high performances were obtained not only in aqueous and organic electrolytes but also in the nonflammable and high-temperature stable ionic liquid electrolyte. Thus, a nonflammable, high-temperature stable ionic-liquid-based supercapacitor was successfully assembled.

Results and Discussion

Figure 1 shows the optical photographs of the reaction liquid at different moments during microwave heating in the preparation of MRG-900-10, and clearly present the state and color change during the reaction process. The reaction liquid was gently boiling because of the intermittent microwave heating technique, and the color deepened from the yellow/brown of the GO precursor at beginning to black after heating for $\geq$6 min due to the efficient reduction from GO to rGO.

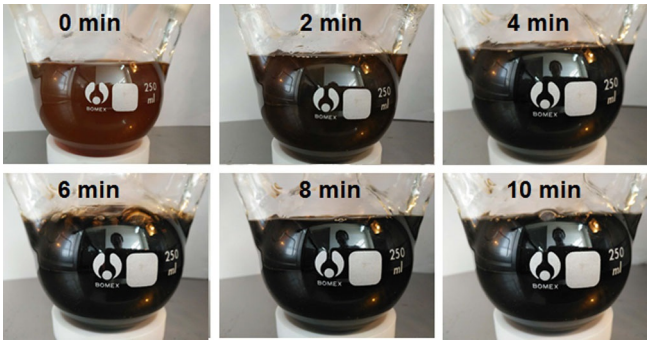

Figure 1. The optical photographs of the reaction liquid at different microwave heating times in the preparation of MRG-900-10.

The morphology and microstructure of the as-prepared MRG-900-10 were characterized by SEM and (HR)TEM in Figure 2. Many rGO slices may be found in Figure 2a. Large-sized rGO nanosheets with several micrometer areas could be clearly seen in Figure 2b. No obvious defects such as holes can be found for the nanosheets based on the TEM image analysis (Figure 2c). The nanosheets are composed of 4–6 monosheets observed from the HRTEM image in Figure 2d. The SEAD pattern image is presented in Figure 2e. The diffraction rings consist of a (002) lattice plane and superposition of the (100) and (101) reflections, that is, (10) lattice plane of the typical polycrystalline graphitic carbon.[14,15]

XRD patterns of GO and the MRGs are shown in Figure 3a. There is a sharp peak at about 11.36° corresponding to the typical (001) reflection of GO. As to the MRGs, the sharp peak disappears completely and two weak broad peaks at about

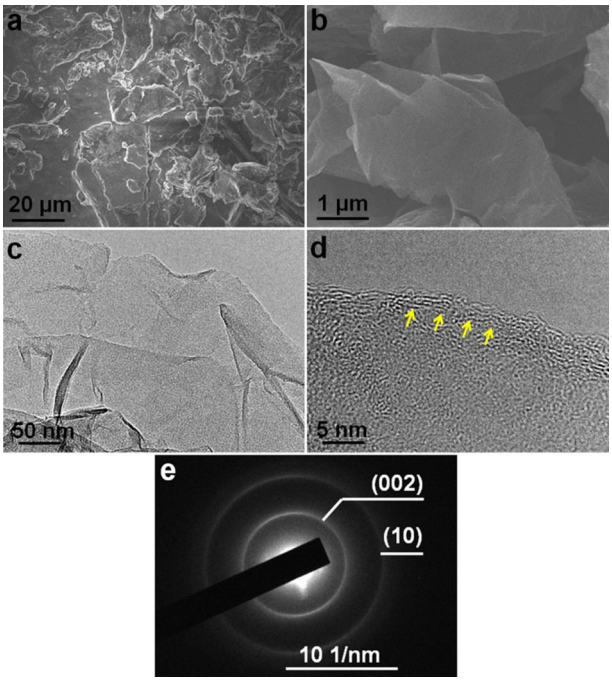

Figure 2. a) and b) SEM images with different magnifications, c) TEM, d) HRTEM, and e) SAED images of the MRG-900-10 sample.

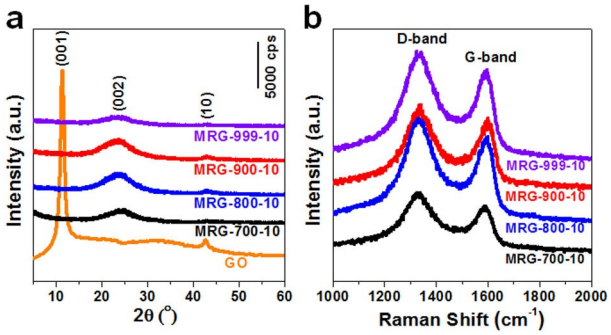

Figure 3. a) XRD patterns and b) Raman spectra of the GO and MRG samples.

24.29 and 42.82° appear due to the (002) and (10) lattice planes of the polycrystalline graphitic carbon, which is consistent with the SEAD analysis. Thus, the GO was well reduced to rGO after the microwave treatment. Raman spectra (Figure 3b) were taken to identify the degree of graphitization of the MRGs. Two peaks at 1340 cm^{-1} (D band) and 1590 cm^{-1} (G band) represent the breathing mode of κ-point phonons with A_{1g} symmetry, which is related to the defective graphitic structure and disordered carbon (sp^3-rich phase), and E_{2g} phonon vibrations of sp^2-bonded carbon atoms, which is a characteristic feature of graphite layers.[16,17] The intensity ratios of I_D/I_G are 1.24, 1.18, 1.15, and 1.18 for MRG-700-10, MRG-800-10, MRG-900-10, and MRG-999-10, respectively, which indicate that defects and structural distortions in the MRG-900-10 sample are the lowest among the MRGs. It can be speculated that low microwave power below 900 W is not enough to form a well-

crystalline structure of MRGs, and high microwave power at 999 W may result in more defects in the structure owning to the too fast heating progress.

The surface functional groups of GO and the MRGs were identified by IR spectra (Figure S1, Supporting Information). The covalently oxygenic groups of O–H (3400), C=O (1730), C–O (1224), C–O–C (1050), and epoxide (860 cm^{-1}) could be found in GO.[18] However, those groups are difficult to observe in the MRGs, due to the reduction under the microwave conditions.

XPS was applied to further identify the elemental contents and carbon related chemical bonds of the MRGs (Figure 4), and the C/O molar ratios as well as the contents of each functional group are shown in Table 1. The XPS C1s spectra of MRGs can be divided into a mainly single peak of sp^2 C (284.8 eV) and other components including C–O (286.5), C=O (288.4), and O=C–O (289.8 eV) as a small tail at the higher-binding energy region.[19,20] The MRG-900-10 has the highest C/O molar ratio (5.89) and the highest content of sp^2 C (69.0%) among the MRGs, which is consistent with the Raman spectral analysis, that is, the MRG-900-10 sample has the lowest defects and structural distortions among the MRGs. Large amounts of sp^2 C and less defective nanosheets can make fast electronic transmission possible. Thus, the MRG-900-10 may have the most efficient electrochemical double-layer capacitance (EDLC) performance and cyclic stability when applied in the supercapacitor.[21–23]

Table 1. The C/O molar ratios as well as the contents of each functional group from the XPS analyses for the MRG samples.

Sample	C/O	sp^2 C [%]	C–O [%]	C=O [%]	O–C=O [%]
MRG-700-10	4.96	36.9	45.6	13.5	3.0
MRG-800-10	5.02	44.2	36.9	14.3	3.0
MRG-900-10	5.89	69.0	18.8	6.3	3.5
MRG-999-10	5.26	35.8	51.3	9.8	2.6

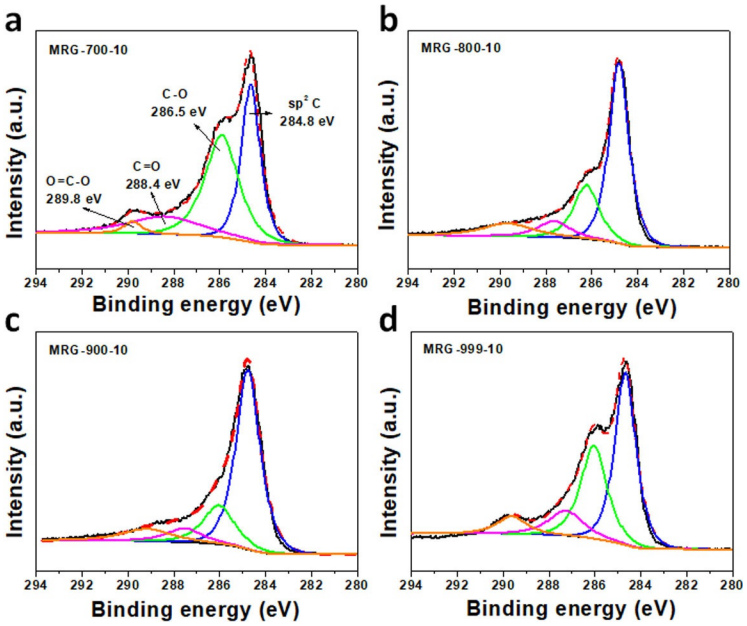

Figure 4. XPS C1s spectra of the MRG samples.

N_2 adsorption–desorption isotherms and the pore-size distributions of the MRGs are shown in Figure 5. The MRGs show type-IV isotherms with sharp adsorption knees at the middle pressure, resulting from the hierarchical porous textures. From the BET results, the specific surface areas are 476.2, 509.9, 568.2, and 754.5 $m^2 g^{-1}$ and the pore volumes are 0.548, 0.580, 0.619, and 0.868 $cm^3 g^{-1}$ for the MRG-700-10, MRG-800-10, MRG-900-10, and MRG-999-10, respectively. The specific surface areas and pore volumes increased along with the rising treated temperature. The large specific surface area can increase the contact surface between the active material and electrolyte, thus the electron and ion transport in the interfaces could be enhanced when they were used as the electrode materials in the supercapacitors. The more specific surface area and pore volume of MRG-999-10 could be caused by the defects such as holes as indicated by the Raman and XPS analyses, which may hinder the fast electronic transmission in the sample. So, the MRG-900-10 will be the best electrode material of the supercapacitor among the MRG samples from the above texture analyses.

The MRG electrodes were tested in a three-electrode configuration in 6 M KOH solutions. Cyclic voltammetry (CV) curves of the MRG-900-10 electrode (Figure 6a) were recorded at different scan rates from 5 to 2000 mV s^{-1}, which can maintain approximately symmetric rectangular shapes with a couple of weakly broadened faradic peaks due to the synergistic effects of EDLC and pseudocapacitance caused

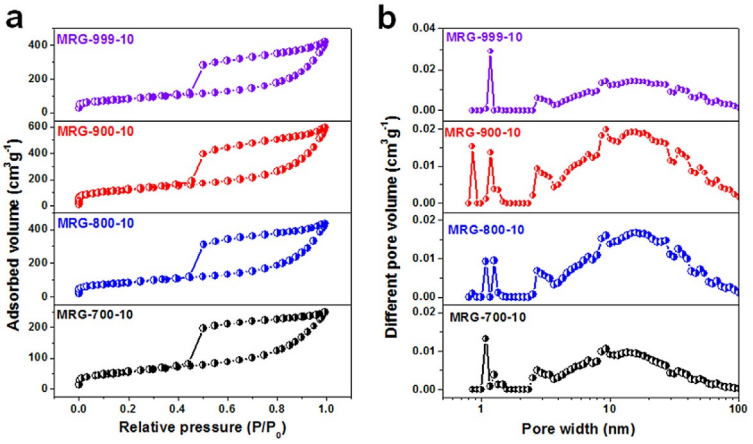

Figure 5. a) N_2 adsorption–desorption isotherms and b) pore-size distributions based on the DFT method for the MRG samples.

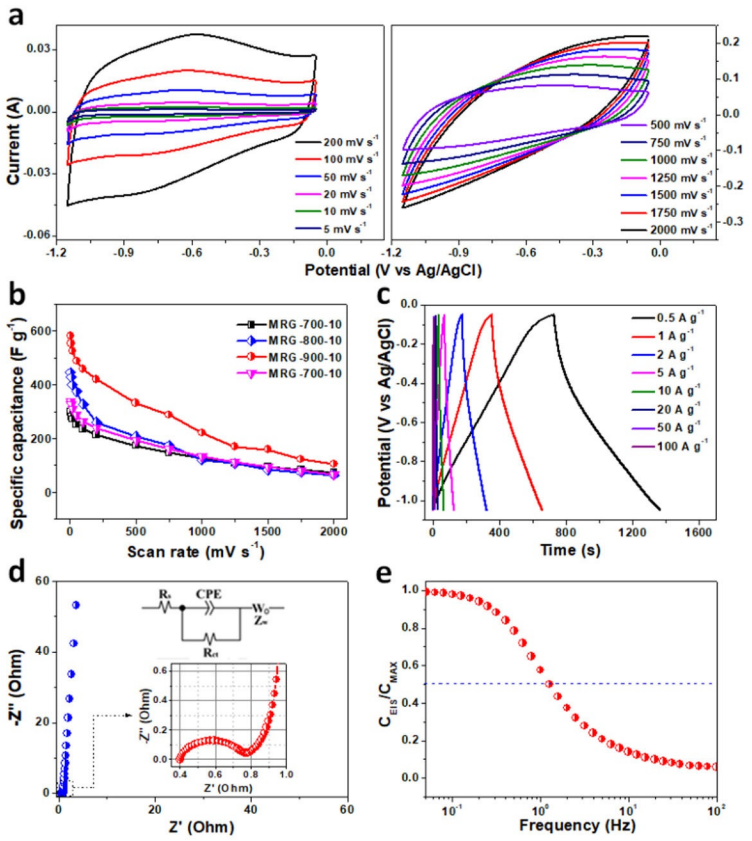

Figure 6. a) CV curves the MRG-900-10 electrodes in 6 M KOH in three-electrode configuration systems; b) the specific capacity of MRG-*x*-10 electrodes calculated from CV curves at different scan rates; c) galvanostatic charge–discharge curves of the MRG-900-10 electrodes in 6 M KOH in a three-electrode configuration system; d) the Nyquist plot with the insets of the plot at high magnification and the equivalent circuit diagram used for the analysis of EIS data of the MRG-900-10 supercapacitor; and e) the frequency response of the gravimetric capacity of the MRG-900-10 supercapacitor.

by the small amount of surface oxygen groups including C=O and C–O, which is consistent with the XPS analyses.[24] The CV curves of the other MRG samples are given in Figure S2, Supporting Information. The specific capacity values are integrated into one chart for comparison (Figure 6b). The MRG-900-10 always has the largest specific capacity among the MRGs at the same scan rates. Galvanostatic charge/discharge tests in the three-electrode configuration were performed to further identify the superior intrinsic capacity performance of MRG-900-10. The almost symmetric triangular-like galvanostatic charge–discharge (GCD) curves (Figure 6c) were obtained at different current densities from 0.5 to 100 A g^{-1}. Typically, the specific capacitance values of 327.6, 287.5, and 248.3 F g^{-1} can be obtained for MRG-900-10 at the current densities of 0.5, 10, and 100 A g^{-1}, respectively, which are very high and even well comparable with some heteroatom-doped carbonaceous electrodes for supercapacitors.[24–29] Besides, the samples prepared at 900 W within different times were tested (Figure S3, Supporting Information) to investigate the effect of heating time on the capacitive properties, and the MRG-900-10 presents the largest specific capacity among the MRG-900-*y* ($y=6$, 8, 10, 12, and 14) samples.

The Nyquist plot is shown in Figure 6d for MRG-900-10 in the 6 M KOH electrolyte. At the low frequency region, the slope of the curve shows the Warburg impedance (*W*), which represents the electrolyte ions diffusion in the porous electrodes. The EIS line is approximately 85° from the actual axis, which is consistent with the typical area of the impedance characteristics of the supercapacitor, indicating that it is very close to the ideal capacitor.[30–33] At high-medium frequency, the short Warburg region indicates a good ion-diffusion efficiency.[34] By extrapolating the vertical line to the real axis, a small value of ESR and charge-transfer resistance (R_{ct}) can be estimated. Concretely, from the first intercept with the real axis in the high frequency region, the equivalent series resistance (ESR) value is 0.4 Ω. The R_{ct} acquired from the diameter of the semicircle in the high-medium frequency region is about 0.36 Ω, which is very low compared to the state-of-the-art carbon based supercapacitors.[35] The low R_{ct} may be a result of the large size and relatively intact (low defects) rGO nanosheet structure, in which the high content of sp^2 C may enhance the electron transport in the layers and the large specific surface area can increase the contact surface area between the active material and the electrolyte, enhancing the electron and ion transport at the interfaces. Thus, the low R_{ct} could lead to an advanced high-power ability of the MRG-900-10 electrode. The Bode plot of the frequency response is shown in Figure 6e. The characteristic frequency f_0 is 1.27 Hz, and the corresponding relaxation time constant τ_0 ($1/f_0$) is accordingly 0.79 s, which is considerably smaller than that of the commercial active carbon-based electrode (≈10 s).[36] The small τ_0 indicates the wide applicable frequency ranges and the faster charge/discharge rates, that is, the good power performance of the MRG-900-10 electrode.[37]

Assembly of MRG 900-10 into a symmetrical supercapacitor in 6 M KOH aqueous electrolyte produced the GCD curves shown in Figure 7. The large specific capacity of 261.9 F g^{-1} could be obtained at the low current density of 0.5 A g^{-1}. A fascinating specific capacity of 79.0 F g^{-1} was gained at a very high current density of 500 A g^{-1}, presenting its advanced high-power characteristic. Moreover, 92% of its initial specific capacity could be maintained after 40 000 cycles at 5 A g^{-1}, indicating the excellent high cyclic stability of the MRG-900-10 supercapacitor (Figure 7d). The inset shows five cycles after 35 000 cycles, which possess pure capacitive behavior inferred from the symmetric GCD curves with hardly any decay after thousands of cycles. Such superior cyclic stability may be attributed to the low R_{ct}[38,39] caused by the large size and low defects rGO nanosheet structure with the high content of sp^2 C and large specific surface area. To gain higher energy densities over broader voltage windows, an organic electrolyte of 1 M tetraethylammonium tetrafluoroborate ([TEA]BF_4)/ACN and ionic liquid electrolytes of 1-ethyl-3-methylimidazolium bis(trifluoromethane)sulfonimide ([EMIM][TFSI])/ACN with different

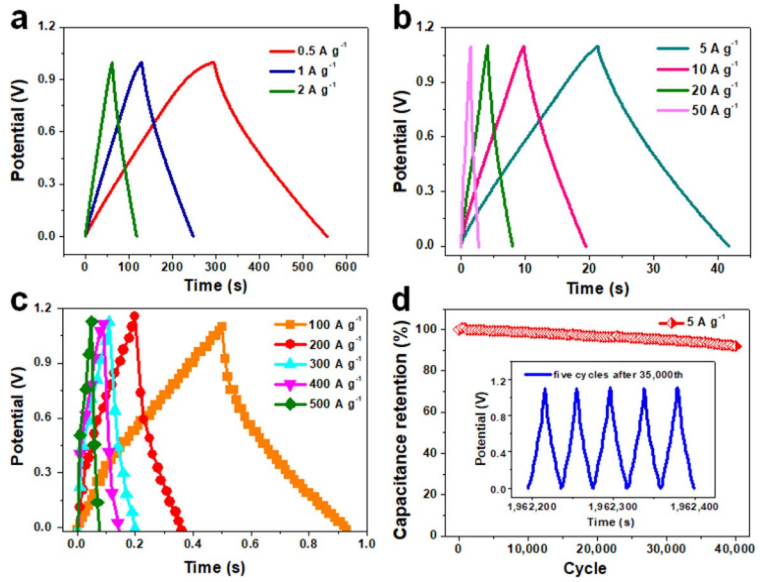

Figure 7. a–c) Galvanostatic charge/discharge curves and d) the long-term cyclic stability of the MRG-900-10 symmetrical supercapacitor in 6 M KOH at a constant current density of 5 A g^{-1} over 40 000 cycles. The inset in (d) shows the GCD curves after 35 000 cycles at a current density of 5 A g^{-1}.

[EMIM][TFSI] volume ratios of 20, 40, 60, 80, and 100 %, named [EMIM][TFSI]-20, 40, 60, 80, and 100, respectively, were chosen to assemble the MRG-900-10 symmetrical supercapacitors. The operating voltage of 1 M [TEA]BF_4/ACN electrolyte was 2.5 V, verified in CV and GCD curves in Figure S4, Supporting Information. As for the [EMIM][TFSI]−*x* electrolytes, the operating voltage expands with the increase of the [EMIM][TFSI] content from the CV curve analyses (Figure S5, Supporting Information). Specifically, the voltage windows of [EMIM][TFSI]-20, 40, 60, 80, and 100 are 2.90, 3.05, 3.25, 3.50, and 3.50 V, respectively. The specific capacities calculated from GCD curves (Figure S6, Supporting Information) at 5 A g^{-1} are shown in Table S1, Supporting Information, and the MRG-900-10 supercapacitor gained the largest specific capacity of 125.2 F g^{-1} in the [EMIM][TFSI]-80 electrolyte. A lower specific capacity obtained in [EMIM][TFSI]-100 is possibly due to the relatively weak adaptability between electrodes and the absolute ionic liquid electrolyte with high viscosity and low wettability.

The Ragone plots of the MRG-900-10 supercapacitor in 6 M KOH aqueous, 1 M [TEA]BF_4/ACN, and [EMIM][TFSI]-80 electrolytes are given in Figure 8. The maximum energy densities of 11.0, 36.2, and 68.6 Wh kg^{-1} could be obtained for MRG 900-10 in the aqueous, organic, and ionic liquid electrolyte systems, respectively, which are obviously superior to that of the typically reported carbon-based supercapacitors.[25–29,40–43] Based on the fact that the active electrode materials approximately accounted for 30 % of the total mass of the commercial supercapacitors or batteries, the normalized practical energy density of the MRG-900-10 supercapacitor in the ionic liquid electrolyte system is estimated to be 22 Wh kg^{-1}, which is much higher than that of the commercial porous activated carbon-based supercapacitors (about 5 Wh kg^{-1})[4] and parallel to that of the usual lead acid batteries (20–30 Wh kg^{-1}).[5,6] Flammability tests on [EMIM][TFSI]−*x* were carried out (Figure 8 b). [EMIM][TFSI]-20, 40, and 60 can be burnt within 1–10 s, whereas [EMIM][TFSI]-80 and 100 are nonflammable. Thus, the fire safety of the supercapacitor in [EMIM][TFSI]-80 electrolyte may be guaranteed. Furthermore, the low volatility and high thermal stability of the ionic liquid electrolyte possibly make it work at high temperatures.[44,45] The CV curves of the MRG-900-10 supercapacitor in [EMIM][TFSI]-80 electrolyte (Figure 8 c) were obtained at between 20 and 100 °C. The specific capacities of 111.4, 114.5, 120.6, 138.9, and 211.6 F g^{-1} were obtained when the temperature was 20, 40, 60, 80, and 100 °C, respectively. The increasing capacities are possibly due to the dissociation of ion pairs at the rising temperature, thus, the activities of ions at the vicinity or electrode/electrolyte interfaces may increase, resulting in the enhanced electric double-layer formation. Besides, the kinetic energy associated with ions in the electrolytes may increase at the rising temperature, which is likely to cause the diffusion of the ions into some inactive holes, increasing the accessible area of active materials. In addition, the pseudocapacitive behavior of residual oxygen functional groups on the rGO is evident when the temperature is enhanced.[46] When the supercapacitor was cooled to room temperature, the CV curve was recovered. Thus, the MRG-900-10 supercapacitor in [EMIM][TFSI]-80 electrolyte can be normally used under the relatively high-temperature conditions up to 100 °C.

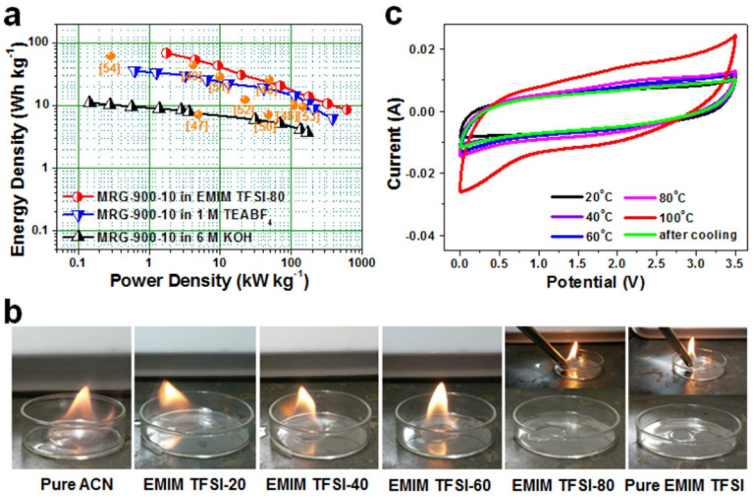

Figure 8. a) The Ragone plots of the MRG-900-10 supercapacitors in 6 M KOH, 1 M [TEA]BF_4/ACN, and 1 M [EMIM]BF_4/ACN electrolyte systems with the typical reported values of the state-of-the-art carbon materials given for comparison; b) flammability tests on the [EMIM][TFSI]-0, 20, 40, 60, 80, and 100 electrolytes; and c) CV curves of the supercapacitor with [EMIM][TFSI]-80 as the electrolyte tested at 20, 40, 60, 80, and 100 °C and after cooling down to room temperature.

Conclusions

Large-sized rGO MRG-900-10 has been synthesized by a fast and efficient intermittent heating microwave reduction method and was separated from a stable dispersion in DMA by choosing ethyl acetate as the precipitant. Large amounts of sp^2 C and less defective nanosheets have been found for the MRG-900-10 sample, which may lead to a fast electronic transmission in the sample. A large specific surface area has been observed for the MRG-900-10 sample, which can increase the contact surface between the active material and the electrolyte, thus the electron and ion transport at the interfaces are enhanced when used as the electrode material in supercapacitors. A low charge-transfer resistance has been obtained for the MRG-900-10 sample, which may not only lead to high performances of MRG-900-10-based supercapacitors in aqueous and organic electrolyte systems, but also make it possible for the assembly of the supercapacitor in ionic liquid electrolyte system even though the electrolyte has a high viscosity and low wettability. High energy density, nonflammablility, and high-temperature stability have been obtained in the optimized ionic liquid [EMIM][TFSI]-80 electrolyte. The advanced electrochemical properties of the MRG-900-10 material are obviously valuable for the supercapacitor utilization especially in extreme conditions, such as fire safety and/or high temperature.

Experimental Section

General

Reagents including $KMnO_4$, $NaNO_3$, KOH, sulfuric acid, DMA, and ethyl acetate were purchased from Beijing Chemical Works. The others were graphite powder (Aladdin, 99.95%), [TEA]BF_4 (Sigma–Aldrich, >97%), [EMIM][TFSI] (Sigma–Aldrich), acetylene black (CABOT BP2000), and poly (vinylidene fluoride) (PVDF) (Arkema HSV900).

GO precursor was prepared from natural graphite powder by the modified Hummer's method.[14] The MRG materials were obtained as follows: Firstly, the as-prepared GO (20 mL, 1.0 mg mL^{-1}) was dispersed into DMA (100 mL), followed by 25 kHz ultrasonic tripping accompanied by magnetic stirring (640 rpm) for 40 min on the Intelligent Temperature Control and Dual Frequency Ultrasonic Synthesizer (XH-2008DE). Secondly, the homogeneous suspension was transferred into a 250 mL three-necked flask, and then moved into the Computerized Microwave Solid-Liquid Phase Synthesizer (XH-200A). The whole heating process was carried out under a N_2 atmosphere. To prevent intense boiling, the Intermittent Heating Technique was chosen, specifically, heating each 1.0 min at the adopted microwave heating power followed by resting for 15 s. A well-dispersed black suspension liquid was obtained under microwave heating at 700, 800, 900, and 999 W, respectively, for 10 min with constant stirring. After cooling to room temperature, the resultant liquid was then transferred to 400 mL beakers, and then 100 mL of ethyl acetate was poured into each beaker, and the flocculent precipitates were separated by centrifugation and dried at 60 °C in an air oven overnight. The obtained samples were named as MRG-*x*-*y* (*x* represents the microwave power, and *y* represents the reaction time). Since the MRG-900-10 sample presented the best electrochemical properties among the MRG-*x*-10 samples, the MRG-900-*y* (*y* = 6, 8, 12, and 14) samples were also prepared by changing the experimental time from 6, 8, 12 to 14 min under the microwave heating at 900 W for comparison.

The micrographs were taken by SEM (Quanta 250 FEG), TEM (JEM-2100), and HRTEM (JEM-2100F). Selected area electron diffraction (SAED) patterns were taken on the JSM-7500F. XRD patterns were determined on the X-ray diffractometer (X-6000) by using $Cu_{K\alpha}$ radiation ($\lambda = 1.5406$ Å) with a scan range from 5 to 60°. Raman spectra were measured on a microscopic confocal Raman spectrometer (LabRAM HR800) by using a 514 nm wavelength laser. The specific surface area and porosity distribution were calculated by the Brunauer–Emmett–Teller (BET) method and DFT model on the basis of nitrogen sorption isotherms measured on a Micromeritics ASAP 2010 analyzer at 77 K. IR spectra were obtained on the microscopic IR spectrometer (iN10MX 750–4000 cm^{-1}). XPS were obtained on the X-ray photoelectron spectrograph (Escalab 250).

Preparations

The working electrode, tested either in a three-electrode configuration or in a two-electrode symmetric supercapacitor, was prepared by mixing 80 wt% MRG, 10 wt% conduction carbon (Super-P), and 10 wt% binder (PVDF) in an *N*-methy-2-pyrrolidone solvent followed by pressing the slurry onto a nickel foam with the electrode printing or dispensing process and then drying at 60 °C for 12 h in a vacuum oven. The weight of active electrode materials was about 2.0 mg cm^{-2}. A typical three-electrode configuration process was carried out with platinum foil and Ag/AgCl as the counter and reference electrodes, respectively, and 6 M KOH aqueous solution as the electrolyte. For the symmetric supercapacitor, two electrodes were partitioned by a porous polypropylene membrane in CR2025-type coin cell, with the electrolytes of 6 M KOH, 1 M [TEA]BF_4/ACN, and a series of [EMIM][TFSI]/ACN ionic liquids, respectively. Galvanostatic charge/discharge (GCD), CV, and electrochemical impedance spectroscopy (EIS) curves were obtained on a CHI 660D electrochemical station, Arbin instruments (BT2143) and GAMRY instruments (Reference 3000). The Bode plot of the frequency response is calculated from the formula of $C_{EIS}(\omega) = -Z''(\omega)/[\omega\,|Z(\omega)|^2]$, $C_{MAX}(\omega) = Z'(\omega)/[\omega\,|Z(\omega)|^2]$, and $C(\omega) = C_{EIS}(\omega) - jC_{MAX}(\omega)$, in which, Z', Z'', and Z are the real, imaginary, and total impedance values [Ω], respectively, with $j = \sqrt{-1}$. C_{EIS}, C_{MAX}, and C represent the real, imaginary, and total capacitances at a specified frequency [F], respectively. The imaginary part of the capacity corresponds to the energy dissipation by irreversible processes. The maximum in the imaginary capacitance-frequency plot represents the dielectric relaxation time of the whole system, in which the frequency response transforms from a resistive to a capacitive one. The results obtained are consistent with the Bode phase plot values, at which f_0 is evaluated. The specific capacity calculated from the CV curves was obtained from the formula of $C = S/(vm\Delta V)$, in which, C is the special capacity, S is the absolute area of CV curve, v is the potential scan rate, m is the mass of active electrode material, and ΔV is the potential window. The specific capacity obtained from the GCD curves was based on the formula of $C = I\Delta t/(m\Delta V)$, in which, I is the discharge current, Δt is the discharge time, m is the active material weight of one electrode, and ΔV is the discharge voltage. The energy density (E) and the power density (P) were calculated by the formulas of $E = C\Delta V^2/8$ and $P = E/\Delta t$, respectively. Besides, the EIS techniques were carried at an open-circuit potential with a perturbation amplitude of 20 mV from 0.01 Hz to 100 kHz.

Acknowledgements

This work was supported by the National Basic Research Programs of China (973 Program, No. 2014CB931800 and 2011CB935700), the Chinese National Science Foundation (No. 21571010 and U0734002), the Chinese Aeronautic Project (No. 2013ZF51069) and 111 Project (No. B14009).

Conflict of interest

The authors declare no conflict of interest.

Keywords: graphene · high-temperature stability · ionic liquids · safety · supercapacitors

[1] L. Zhang, X. Zhao, *Chem. Soc. Rev.* **2009**, *38*, 2520 – 2531.
[2] L.-Z. Guan, L. Zhao, Y.-J. Wan, L.-C. Tang, *Nanoscale* **2018**, *10*, 14788 – 14811.
[3] D. A. C. Brownson, D. K. Kampouris, C. E. Banks, *J. Power Sources* **2011**, *196*, 4873 – 4885.
[4] A. Burke, *Electrochim. Acta* **2007**, *53*, 1083 – 1091.
[5] L. Shen, H. Lv, S. Chen, P. Kopold, P. A. Aken, X. Wu, J. Maier, Y. Yu, *Adv. Mater.* **2017**, *29*, 1700142.
[6] J. Xu, J. Ma, Q. Fan, S. Guo, S. Dou, *Adv. Mater.* **2017**, *29*, 1606454.
[7] Z. Quan, E. Ni, S. Hayashi, N. Sonoyama, *J. Mater. Chem. A* **2013**, *1*, 8848 – 8856.
[8] K. Chen, S. Song, D. Xue, *J. Mater. Chem. A* **2015**, *3*, 2441 – 2453.
[9] P. Liu, T. Yan, L. Shi, H. Park, X. Chen, Z, Zhao, D. Zhang, *J. Mater. Chem. A* **2017**, *5*, 13907 – 13943.
[10] H. Feng, R. Cheng, X. Zhao, X. Duan, J. Li, *Nat. Commun.* **2013**, *4*, 1539 – 1556.
[11] J. Cai, P. Ruffieux, R. Jaafar, M. Bieri, T. Braun, S. Blankenburg, M. Muoth, A. P. Seitsonen, M. Saleh, X. Feng, K. Müllen, R. Fasel, *Nature* **2010**, *466*, 470 – 473.
[12] Y. Zhu, S. Murali, M. D. Stoller, A. Velamakanni, R. D. Piner, P. S. Ruoff, *Carbon* **2010**, *48*, 2106 – 2122.
[13] F. Zhang, T. Zhang, X. Yang, L. Zhang, K. Leng, Y. Huang, Y. Chen, *Energy Environ. Sci.* **2013**, *6*, 1623 – 1632.
[14] H. Wang, Z. Xu, A. Kohandehghan, Z. Li, K. Cui, X. Tan, T. J. Stephenson, C. K. King'ondu, C. M. B. Hollt, B. C. Olsen, J. K. Tak, D. Harfield, A. O. Anyia, D. Mitlin, *ACS Nano* **2013**, *7*, 5131 – 5141.
[15] H. Wang, Z. Xu, Z. Li, K. Cui, J. Ding, A. Kohandehghan, X. Tan, B. Zahiri, B. C. Olsen, C. M. B. Holt, D. Mitlin, *Nano Lett.* **2014**, *14*, 1987 – 1994.
[16] M. Sevilla, A. B. Fuertes, *ACS Nano* **2014**, *8*, 5069 – 5078.
[17] J. Hou, C. Cao, F. Idrees, X. Ma, *ACS Nano* **2015**, *9*, 2556 – 2564.
[18] S. Park, J. An, I. Jung, R. D. Piner, S. J. An, X. Li, A. Velamakanni, R. S. Ruoff, *Nano Lett.* **2009**, *9*, 1593 – 1597.
[19] D. C. Marcano, D. V. Kosynkin, J. M. Berlin, A. Sinitskii, Z. Sun, A. Slesarev, L. B. Alemany, W. Lu, J. M. Tour, *ACS Nano* **2010**, *4*, 4806 – 4814.
[20] B. Xu, S. Yue, Z. Sui, X. Zhang, S. Hou, G. Cao, Y. Yang, *Energy Environ. Sci.* **2011**, *4*, 2826 – 2830.
[21] Z. Lei, L. Lu, X. S. Zhao, *Energy Environ. Sci.* **2012**, *5*, 6391 – 6399.
[22] E. Raymundo-Piñero, F. Leroux, F. Béguin, *Adv. Mater.* **2006**, *18*, 1877 – 1882.
[23] H. Zhu, X. Wang, X. Liu, X. Yang, *Adv. Mater.* **2012**, *24*, 6524 – 6529.
[24] Y. Fang, B. Luo, Y. Jia, X. Li, B. Wang, Q. Song, F. Kang, L. Zhi, *Adv. Mater.* **2012**, *24*, 6348 – 6355.
[25] L. Zhang, X. Zhao, M. D. Stoller, Y. Zhu, H. Ji, S. Murali, Y. Wu, S. Perales, B. Clevenger, R. S. Ruoff, *Nano Lett.* **2012**, *12*, 1806 – 1812.
[26] Y. Wang, Z. Shi, Y. Huang, Y. Ma, C. Wang, M. Chen, Y. Chen, *J. Phys. Chem. C* **2009**, *113*, 13103 – 13107.
[27] J. Zhang, J. Jiang, H. Li, X. S. Zhao, *Energy Environ. Sci.* **2011**, *4*, 4009 – 4015.
[28] W. Tian, Q. Gao, Y. Tan, Y. Zhang, J. Xu, Z. Li, K. Yang, L. Zhu, Z. Liu, *Carbon* **2015**, *85*, 351 – 362.
[29] L. Qie, W. Chen, H. Xu, X. Xiong, Y. Jiang, F. Zou, X. Hu, Y. Xin, Z. Zhang, Y. Huang, *Energy Environ. Sci.* **2013**, *6*, 2497 – 2504.
[30] E. Raymundo-Piñero, F. Leroux, M. Cadek, F. Béguin, *Adv. Funct. Mater.* **2009**, *19*, 1032 – 1039.
[31] C. Largeot, C. Portet, J. Chmiola, P. Taberna, Y. Gogotsi, P. Simon, *J. Am. Chem. Soc.* **2008**, *130*, 2730 – 2731.
[32] L. Zhang, D. DeArmond, N. T. Alvarea, D. Zhao, T. Wang, G. Hou, R. Malik, W. R. Heineman, V. Shanov, *J. Mater. Chem. A* **2016**, *4*, 1876 – 1886.
[33] R. Kötz, M. Carlen, *Electrochim. Acta* **2000**, *45*, 2483 – 2498.
[34] M. Arulepp, L. Permann, J. Leis, A. Perkson, K. Rumma, A. Jänes, E. Lust, *J. Power Sources* **2004**, *133*, 320 – 328.
[35] S. Nardecchia, D. Carriazo, M. L. Ferrer, M. C. Gutiérrez, F. Monte, *Chem. Soc. Rev.* **2013**, *42*, 794 – 830.
[36] P. L. Taberna, P. Simon, J. F. Fauvarque, *J. Electrochem. Soc.* **2003**, *150*, A292 – A300.
[37] J. Gamby, P. L. Taberna, P. Simon, J. F. Fauvarque, M. Chesneau, *J. Power Sources* **2001**, *101*, 109 – 116.
[38] W. Qian, F. Sun, Y. Xu, L. Qiu, C. Liu, S. Wang, F. Yan, *Energy Environ. Sci.* **2014**, *7*, 379 – 386.
[39] V. Ganesh, S. Pitchumani, V. Lakshminarayanan, *J. Power Sources* **2006**, *158*, 1523 – 1532.
[40] Y. Gogotsi, P. Simon, *Science* **2011**, *334*, 917 – 918.
[41] Z. Wu, W. Ren, D. Wang, F. Li, B. Liu, H. Cheng, *ACS Nano* **2010**, *4*, 5835 – 5842.
[42] P. Chen, G. Shen, Y. Shi, H. Chen, C. Zhou, *ACS Nano* **2010**, *4*, 4403 – 4411.
[43] W. Tian, Q. Gao, L. Zhang, C. Yang, Z. Li, Y. Tan, W. Qian, H. Zhang, *J. Mater. Chem. A* **2016**, *4*, 8690 – 8699.
[44] X. Li, T. Li, Q. Zhong, K. Du, H. Li, J. Huang, *Electrochim. Acta* **2014**, *125*, 170 – 175.
[45] T. Chen, L. Dai, *J. Mater. Chem. A* **2014**, *2*, 10756 – 10775.
[46] F. Liu, S. Song, D. Xue, H. Zhang, *Adv. Mater.* **2012**, *24*, 1089 – 1094.

Manuscript received: August 27, 2018
Revised manuscript received: September 19, 2018
Accepted manuscript online: September 21, 2018
Version of record online: November 7, 2018